Contrib. Astron. Obs. Skalnaté Pleso **57/1**, 7 – 26, (2027)
https://doi.org/10.31577/caosp.2027.57.1.7

# TESS periodic variability of kinematically selected nearby high-velocity dwarfs from GCNS and Gaia DR3

**F. Li**[1] **and G. Huang**[2]

[1] *School of Artificial Intelligence, Nanjing Vocational College of Information Technology, Nanjing, China, (E-mail: liff@njcit.cn) (corresponding author)*

[2] *College of Information Engineering, Northwest A&F University, Yangling, China, (E-mail: harry.huang@nwafu.edu.cn)*

Received: August 11, 2026; Accepted: September 11, 2026

**Abstract.** This study searches Transiting Exoplanet Survey Satellite (TESS) light curves for periodic photometric variability among kinematically selected nearby high-velocity dwarfs. Space motions recomputed from the Gaia Catalogue of Nearby Stars (GCNS) and Gaia DR3 yield a parent sample of 182 dwarf candidates with total velocity relative to the local standard of rest $v_{\rm LSR} \geq 180\,{\rm km\,s^{-1}}$. A brightness-prioritised archive search of the 100 brightest candidates provides usable TESS data for a 98-target subsample, to which all detection yields refer. Lomb–Scargle periodograms over 0.1–13 d are evaluated for 227 sector light curves after screening signals near the search boundaries and the harmonics of the spacecraft orbital period. Fourteen targets show consistent periods in multiple sectors and form the primary candidate tier; ten further targets with strong single-sector signals form a secondary, less confirmed tier. Candidate periods range from 1.668 to 8.600 d and are reported as periodic photometric variability rather than as confirmed rotation periods. Only one primary candidate has a period shorter than 2 d; its TESS aperture also contains a GCNS-bound companion at 2.76 arcsec, and the system is flagged for resolved follow-up. No significant correlations are found between period and LSR velocity, Gaia colour, or absolute $G$ magnitude, and an exploratory test of a catalogue multiplicity indicator shows no statistically significant association with period detection (odds ratio 2.41; Fisher $p = 0.189$). An indicative injection–recovery test on eight representative light curves shows high sensitivity to the tested short-period signals at a semi-amplitude of about 0.03 per cent, with marked incompleteness below 0.01 per cent. Period consistency, alias rejection, and the sensitivity test together define a compact candidate catalogue for high-spatial-resolution photometric and spectroscopic follow-up.

**Key words:** stars: rotation – stars: kinematics and dynamics – stars: low-mass – binaries: general – methods: data analysis – techniques: photometric

[1]Correspondence and material requests should be addressed to F. Li (E-mail: liff@njcit.cn).

## 1. Introduction

Angular-momentum loss through magnetised winds links the rotation of cool main-sequence stars to their evolution. The empirical spin-down relation first identified by Skumanich (1972) motivated gyrochronology calibrations in which rotation period is interpreted jointly with stellar colour or mass (Barnes, 2007; Mamajek & Hillenbrand, 2008). Subsequent work has shown that the mapping is neither universal nor monotonic over every evolutionary regime. Asteroseismic calibrators expose substantial late-age scatter (Angus et al., 2015), and weakened magnetic braking may leave some old field stars rotating faster than classical prescriptions predict (van Saders et al., 2016). Short periods among old-population candidates are accordingly interesting, but their interpretation requires more than a single period measurement.

Galactic kinematics supplies a complementary, population-level view of stellar age. Velocity dispersion grows statistically with the age of a disc population, and nearby M-dwarf surveys have related their rotation distributions to Galactic motions (Newton et al., 2016; Giacobbe et al., 2020). Large space velocity does not determine the age or chemical population of an individual star; it instead identifies a kinematically hot sample in which rapid modulation is comparatively unusual. Such modulation may arise from an atypical single star, a close binary, a spotted companion, or an unresolved source unrelated to the target. Harmonic structure can also place a measured photometric period at one half or twice the rotation period.

Gaia and TESS make a direct search across this regime possible. Positions, parallaxes, proper motions, photometry, and radial velocities from Gaia DR3 support a homogeneous three-dimensional kinematic selection (Gaia Collaboration et al., 2023; Katz et al., 2023). The GCNS complements those data with a probabilistically selected nearby-star inventory and resolved-pair information (Gaia Collaboration et al., 2021). TESS then supplies repeated, high-cadence photometry across much of the sky (Ricker et al., 2015). In the present analysis, the Gaia products define the stars to be examined, whereas TESS provides an independent time-domain measurement.

Gaia DR3 has also been combined with the LAMOST spectroscopic survey to study high-velocity stars on Galactic scales. Elsanhoury (2025) analysed three LAMOST–Gaia DR3 high-velocity samples of 591, 87, and 519 stars at distances from about 0.1 to 109 kpc and derived their space velocities, velocity-ellipsoid dispersions, convergent points, solar motion, and Galactic rotation parameters. Li et al. (2026) reassessed three published Gaia–LAMOST high-velocity-star catalogues and showed that the unbound classification of their candidates depends chiefly on the adopted distance estimator. Those studies treat high-velocity stars as kinematic tracers of the Galaxy. The present work addresses a complementary, time-domain question: a volume-limited nearby sample is defined from GCNS and Gaia DR3 alone, without spectroscopic-survey membership, and the individual

stars are then examined for periodic photometric variability with TESS. Sect. 4 returns to this comparison.

Photometric rotation studies infer a period from the changing visibility of starspots and active regions. Large Kepler catalogues established the power of this approach for cool dwarfs (McQuillan et al., 2014), although blind recovery experiments also demonstrated that spot evolution, differential rotation, and analysis choices can generate aliases or missed detections (Aigrain et al., 2015). TESS measurements add a different window function: most sectors cover only a few weeks, and repeated sectors can be separated by months or years. Agreement between independent sectors is therefore valuable evidence that a peak is not tied to a particular instrumental trend or a short-lived light-curve feature (Binks & Günther, 2024).

Spatial blending presents an additional concern. A TESS pixel spans about 21 arcsec, large enough for several Gaia sources to contribute to one photometric aperture (Stassun et al., 2019). The spacecraft's 13.7-d orbit, the finite sector baseline, and common half/double-period ambiguities further complicate the period spectrum. Neighbour searches, boundary checks, harmonic comparisons, and cross-sector repeatability consequently form part of the measurement rather than optional post-processing. These checks are especially important for the low-amplitude signals expected from older or weakly spotted stars (Binks et al., 2022; Binks & Günther, 2024).

Earlier work found few very short periods among kinematically older nearby M dwarfs (Giacobbe et al., 2020), whereas targeted TESS observations have characterised selected ultrafast low-mass rotators (Ramsay et al., 2020). Nearby high-velocity dwarfs occupy the overlap between these lines of investigation, but a validated TESS search of such objects remains limited. Three questions guide this study: how many targets show repeatable or otherwise strong periodic photometric variability; whether any candidates have periods shorter than 2 d; and whether period is associated with kinematics, colour, luminosity, or catalogue multiplicity indicators. Throughout, a detected period is treated as periodic photometric variability of the light within the TESS aperture. It identifies a rotation candidate, not a measured rotation period, unless independent evidence supports a rotational origin. Multi-sector and single-sector evidence are kept in separate tiers, and the final catalogue records alias, neighbour, and injection–recovery diagnostics.

## 2. Data and methods

### 2.1. Nearby-star parent sample and Gaia DR3 update

Construction of the parent sample began with the reliable-source table of the GCNS (Gaia Collaboration et al., 2021). Valid Gaia photometry, a published radial velocity, and a positive parallax were required. Objects clearly displaced from the dwarf sequence were removed through a broad locus in the $M_G$–($G_{\rm BP}$ –

$G_{\rm RP}$) diagram. Measurement-quality and observing-range cuts then required a parallax signal-to-noise ratio of at least 10, radial-velocity uncertainty below $10\,\mathrm{km\,s^{-1}}$, $6 \le G \le 14$ mag, and $0.5 \le G_{\rm BP} - G_{\rm RP} \le 1.8$ mag.

A tangential-velocity threshold of $120\,\mathrm{km\,s^{-1}}$reduced the number of archive queries before the full three-dimensional calculation. With total proper motion $\mu = (\mu_{\alpha*}^2 + \mu_\delta^2)^{1/2}$ and parallax $\varpi$, both in milliarcseconds, the preselection quantity was

$$v_{\rm tan} = 4.74047\,\frac{\mu}{\varpi} \quad \mathrm{km\,s^{-1}}. \tag{1}$$

This lower threshold was used only to avoid querying stars that could not plausibly enter the final high-velocity sample.

Each preselected identifier was subsequently matched to Gaia DR3. Published DR3 astrometric parameters and radial velocities replaced the EDR3 values used in the original GCNS calculations. Transformation of the six-dimensional observables into heliocentric Galactic Cartesian velocities $(U, V, W)$ was performed with Astropy (Astropy Collaboration et al., 2022). Following Schönrich et al. (2010), the adopted solar peculiar motion was

$$(U, V, W)_\odot = (11.1, 12.24, 7.25)\,\mathrm{km\,s^{-1}} \tag{2}$$

relative to the local standard of rest (LSR). The selection speed is therefore

$$v_{\rm LSR} = \left(U_{\rm LSR}^2 + V_{\rm LSR}^2 + W_{\rm LSR}^2\right)^{1/2}. \tag{3}$$

Membership in the primary sample requires $v_{\rm LSR} \ge 180\,\mathrm{km\,s^{-1}}$ and RUWE $< 2.0$; a stricter RUWE $< 1.4$ subset was retained for a sensitivity check. After the DR3 update, 182 stars satisfy the primary criteria. These two conditions, $v_{\rm LSR} \ge 180\,\mathrm{km\,s^{-1}}$ and RUWE $< 2.0$, define the parent sample referred to throughout the paper. Figure 1 and Table 1 summarise the selection sequence.

**Table 1.** Sample-construction funnel.

| Selection stage | Number |
|---|---|
| GCNS reliable catalogue | 331,312 |
| Photometry/RV/basic quality | 52,314 |
| Broad dwarf locus | 47,268 |
| Inclusive astrometry | 37,940 |
| GCNS speed $\ge 180$ km s$^{-1}$ | 225 |
| Strict RUWE $< 1.4$ | 214 |
| Updated Gaia DR3 speed $\ge 180$ km s$^{-1}$ | 182 |
| TESS light curve available | 98 |
| Periodic candidate (either tier) | 24 |

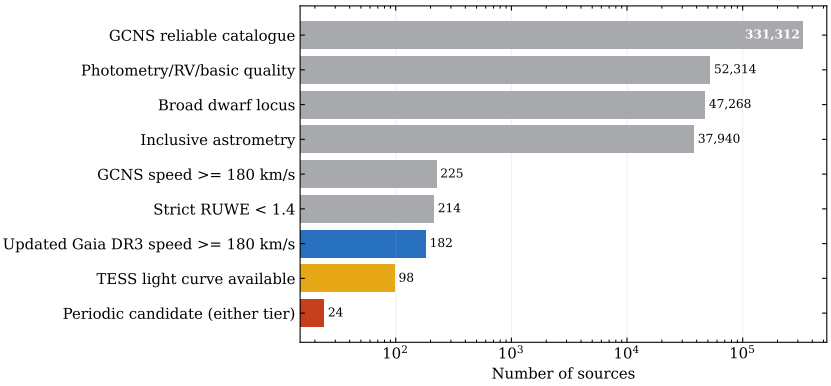



**Figure 1.** Sample construction from the GCNS parent catalogue to the 182-star Gaia DR3 parent sample, the brightness-prioritised 98-target TESS subsample, and the 24 periodic-variability candidates of both evidence tiers.

### 2.2. TESS products and light-curve preparation

Archive acquisition followed Gaia $G$ magnitude, from bright to faint. The 100 brightest of the 182 parent-sample candidates were queried in the Mikulski Archive for Space Telescopes using a 20-arcsec search radius centred on the Gaia DR3 catalogue coordinates. A light curve was retained only when its product coordinates lay within 3 arcsec of the target. If several products existed for one sector, a single product was chosen in the order SPOC, TESS-SPOC, QLP, TASOC, and TARS. The resulting TESS subsample contains 98 targets. Because retrieval was limited to the 100 brightest candidates, this subsample is magnitude-selected rather than representative of the parent sample, and the remaining 84 candidates were not searched. All detection yields quoted below therefore refer to the 98-target TESS subsample and not to the 182-star parent sample.

Lightkurve (Lightkurve Collaboration et al., 2018) provided a common interface to the different high-level products. SPOC and TESS-SPOC light curves used PDCSAP flux generated by the mission pipeline (Jenkins et al., 2016); its cotrending framework is derived from the Kepler Presearch Data Conditioning algorithms (Stumpe et al., 2012; Smith et al., 2012). For QLP, TASOC, and other high-level products, the calibrated flux supplied by the respective archive product was adopted (Huang et al., 2020; Handberg et al., 2021). Non-finite measurements and cadences with non-zero quality flags were discarded.

Numerical analysis required at least 500 valid cadences and an observing baseline of 10 d. For an accepted sector, flux was converted to relative units

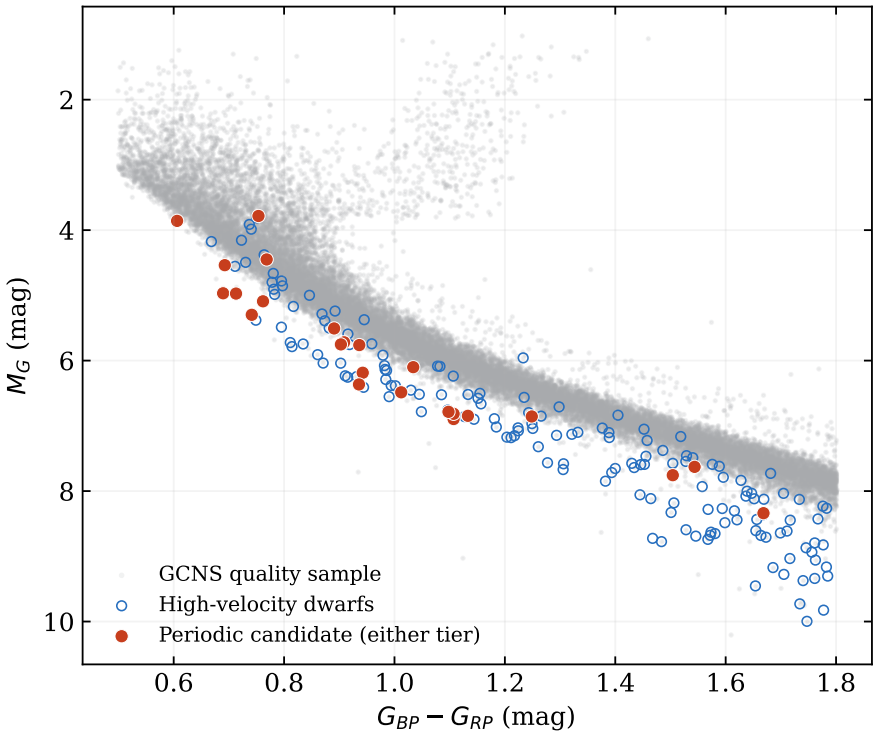



**Figure 2.** Gaia DR3 colour–absolute-magnitude diagram. Symbols distinguish the 182-star parent sample, the 98-target TESS subsample, and the periodic-variability candidates of either tier. The broad dwarf region shown here was used for the initial sample selection.

according to

$$y_i = \frac{F_i}{\mathrm{median}(F)} - 1. \tag{4}$$

A linear trend was removed before and after outlier clipping. If $r_i$ denotes the residuals after the first detrending pass, the robust scale was

$$\sigma_{\mathrm{MAD}} = 1.4826 \ \mathrm{median}\,|r_i - \mathrm{median}(r)|\,, \tag{5}$$

and points farther than $6\sigma_{\mathrm{MAD}}$ from the residual median were excluded. No information from another sector entered this detrending step. CROWDSAP, when present, was retained as an aperture-contamination diagnostic. The frozen analysis list contains 229 products; 227 sector light curves passed the cadence, baseline, and numerical checks.

### 2.3. Period search and evidence tiers

Unevenly sampled periodicity was evaluated with the Lomb–Scargle formalism (Lomb, 1976; Scargle, 1982; VanderPlas, 2018). For a sector of valid duration $\Delta T$, Lightkurve computed the periodogram over $0.1 \leq P \leq \min(13, \Delta T/3)$ d. The upper bound ensures that every trial period is represented by at least three cycles. At each frequency $f$, the fitted model has the form

$$m(t; f) = c + a\cos(2\pi f t) + b\sin(2\pi f t). \tag{6}$$

Peak significance was measured with the Baluev analytic false-alarm probability (Baluev, 2008). A sector-level detection required FAP $< 10^{-3}$, at least three observed cycles, and a coherent-amplitude signal-to-noise ratio of at least 3.

Two diagnostics were calculated from the best-fitting model. Its reported semi-amplitude is half the difference between the 95th and 5th percentiles of $m(t; f)$, and the coherent-amplitude statistic is

$$A = \frac{Q_{95}(m) - Q_5(m)}{2}, \qquad S_A = \frac{A}{\sigma_{\mathrm{MAD}}}\sqrt{\frac{N}{2}}, \tag{7}$$

where $N$ is the number of retained cadences and $\sigma_{\mathrm{MAD}}$ is recomputed from the post-fit residuals. This statistic distinguishes a coherent low-amplitude signal measured over many cadences from a fluctuation comparable to the point-to-point scatter.

Candidate classification also incorporated explicit vetoes. Peaks within two per cent of either search boundary were rejected. Fixed windows around 0.5, 1.0, and 2.0 d were flagged as likely aliases. The 13.7-d TESS orbital period was treated as follows. Because the upper search limit never exceeds 13 d, the orbital period itself lies outside the searched range and cannot be selected as a periodogram maximum. Its low-order harmonics at $13.7/n$ d for $n = 2$–$5$ (6.85, 4.57, 3.43, and 2.74 d) do fall inside the range; a maximum was flagged as orbit-related whenever it lay within the larger of 0.04 d or 2.5 per cent of one of these harmonic periods, and the same window was applied to the fundamental for completeness. Residual orbit-related power at periods approaching the upper limit is removed by the boundary veto. Flagged maxima remain available for diagnostic plots but do not independently establish a candidate.

For a star observed in several sectors, significant periods were compared after mapping each measurement onto the $P/2$, $P$, or $2P$ harmonic closest to a candidate consensus. The primary multi-sector tier requires at least two mapped periods to agree within 10 per cent. Their median defines the target period $\widetilde{P}$, and the tabulated fractional scatter is

$$s_P = \frac{\mathrm{std}(P_k)}{\widetilde{P}}. \tag{8}$$

Significant peaks that fail this agreement rule are labelled inconsistent multi-sector results. A target with only one usable sector enters the secondary strong-single-sector tier when FAP $< 10^{-8}$, $S_A \geq 6$, and neither a boundary nor an

alias flag is present. Weaker single-sector signals and non-detections complete the target-level classification. The two tiers carry different levels of observational confirmation and are called primary and secondary candidates throughout; wherever they are counted together, the text refers explicitly to candidates of both tiers.

### 2.4. Association tests and injection–recovery experiment

Exploratory Spearman tests compared candidate period with $v_{\rm LSR}$, $G_{\rm BP} - G_{\rm RP}$, and $M_G$. Benjamini–Hochberg adjustment was applied to the three resulting $p$ values. A separate multiplicity indicator combined Gaia DR3 non-single-star solutions, radial-velocity variability inferred from the published goodness-of-fit fields, and resolved GCNS pairs. Its association with candidate detection over all 98 TESS targets was evaluated by a two-sided Fisher exact test. Both the correlation tests and the multiplicity comparison are exploratory screens; the sample was not designed to establish an association. Neighbouring Gaia sources around the shortest-period candidate were also cross-checked against the GCNS pair table.

Detection sensitivity was estimated by injecting sinusoids into eight real residual light curves spanning the brightness range. Original time sampling and correlated residual noise were preserved. Five periods (0.25, 0.7, 1.3, 2.3, and 5.0 d), five fractional semi-amplitudes ($10^{-5}$ to $10^{-3}$), and five trials per light curve produced 1000 injections. A recovery required FAP $< 10^{-3}$ and agreement with the injected period to within 10 per cent after allowing the $P/2$, $P$, and $2P$ alternatives. For every grid cell, the reported completeness is

$$R(P, A) = \frac{N_{\rm recovered}(P, A)}{N_{\rm injected}(P, A)}. \tag{9}$$

This design follows the general use of blind or injection-based tests to expose period-dependent failures that are not represented by analytic false-alarm probabilities alone (Aigrain et al., 2015). Because it samples eight light curves and one sinusoidal signal shape, the experiment is an indicative sensitivity test of the adopted pipeline rather than a population-level completeness analysis; Sect. 4 discusses this scope.

## 3. Results

### 3.1. Kinematic and photometric samples

After the Gaia DR3 update and kinematic selection, the parent sample contains 182 stars spanning 9.2–100.4 pc (median 78.8 pc). Its median magnitude, colour, and LSR speed are $G = 11.31$, $G_{\rm BP} - G_{\rm RP} = 1.25$, and $v_{\rm LSR} = 248.8\,{\rm km\,s^{-1}}$, respectively; individual speeds range from 180.1 to 594.1 $\rm km\,s^{-1}$. As illustrated

by Fig. 2, most objects occupy the adopted dwarf-sequence region. Periodic-variability candidates are distributed across the parent sample's broad kinematic locus in Fig. 3, with no marked concentration towards its low-velocity edge.

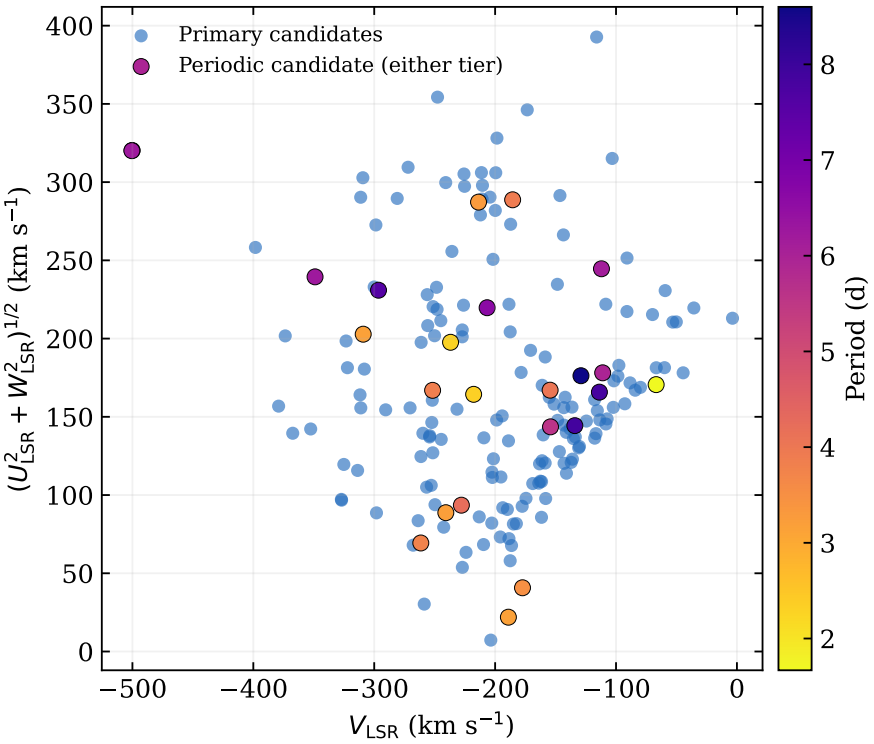



**Figure 3.** Toomre-style kinematic projection of the 182-star Gaia DR3 parent sample. Periodic-variability candidates of either tier are coloured by their consensus periods.

Usable TESS products were retrieved for 98 of the 182 candidates in the brightness-prioritised search; the remaining 84 fainter candidates were not searched. These 98 targets form the TESS subsample to which every yield below refers. Ninety-three of them also satisfy the stricter RUWE $< 1.4$ criterion, as do all 24 periodic-variability candidates of both tiers introduced in Sect. 3.2.

### 3.2. Period-evidence tiers

Fourteen targets satisfy the multi-sector criterion and constitute the primary candidates. Ten additional objects meet the strong-single-sector criterion and constitute the secondary candidates, whose periods await confirmation in a

second sector. Among the remainder are 20 inconsistent multi-sector results, 33 weaker single-sector signals, and 21 objects without a significant detection. Within the TESS subsample, the combined yield of primary and secondary candidates is 24/98 = 24.5 per cent (Wilson 95 per cent interval 17.0–33.9 per cent), and the primary-tier yield is 14/98 = 14.3 per cent (8.7–22.6 per cent). These fractions describe the magnitude-selected 98-target subsample; they are not estimates of the periodic-variable fraction of the 182-star parent sample.

Across both tiers, periods extend from 1.668 to 8.600 d and have a median of 4.130 d. Fitted semi-amplitudes cover 0.0065–4.626 per cent, with a median of 0.0287 per cent. Period, amplitude, colour, and kinematic properties are compared in Fig. 4. The 14 primary candidates are listed in Table 2; Table A1 and its machine-readable counterpart contain the full 24-object catalogue with the tier of each entry. All periods are reported as periodic photometric variability of the light within the TESS aperture; none is claimed as a confirmed rotation period.

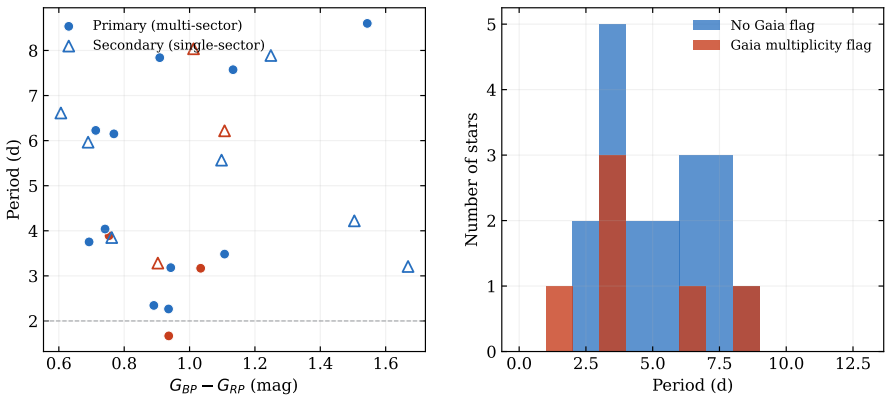



**Figure 4.** Properties of the 24 periodic-variability candidates. Filled circles mark primary (multi-sector) candidates and open triangles mark secondary (strong-single–sector) candidates; colours indicate the catalogue multiplicity indicator. The horizontal line at 2 d marks the predefined fast-candidate threshold.

Only Gaia DR3 2112434245261736192, a primary candidate, falls below the predefined 2-d threshold. Two sectors support its consensus period of $P$ = 1.6682 d, with a fractional period scatter of 0.038 and a fitted semi-amplitude of 0.0248 per cent. Target-level diagnostics (Fig. 5) reveal the recurring periodogram peak and its low-amplitude phase modulation.

A neighbouring Gaia source, 2112434039101770624, lies 2.763 arcsec from this target and is fainter by $\Delta G$ = 3.733 mag. Its approximate contribution

**Table 2.** Primary candidates: targets with multi-sector-consistent periodic photometric variability.

| Gaia DR3 source ID | $G$ (mag) | $G_{\rm BP} - G_{\rm RP}$ (mag) | $v_{\rm LSR}$ (km s$^{-1}$) | $P$ (d) | Support (sectors) | $\sigma_P/P$ | Semi-amp. (%) | Mult. |
|---|---|---|---|---|---|---|---|---|
| 2112434245261736192 | 10.66 | 0.94 | 183.2 | 1.668 | 2 | 0.038 | 0.025 | Y |
| 1080623048803799040 | 11.32 | 0.94 | 308.5 | 2.265 | 2 | 0.040 | 0.028 | N |
| 6480032187014809600 | 10.06 | 0.89 | 272.8 | 2.344 | 2 | 0.049 | 0.019 | N |
| 5380306876026603648 | 8.67 | 1.03 | 190.3 | 3.169 | 2 | 0.047 | 0.023 | Y |
| 5817597047142573952 | 10.70 | 0.94 | 369.7 | 3.182 | 2 | 0.038 | 0.019 | N |
| 219057458247921536 | 8.23 | 1.11 | 182.0 | 3.483 | 2 | 0.052 | 0.024 | N |
| 1752459532807704704 | 8.21 | 0.69 | 270.5 | 3.753 | 2 | 0.025 | 0.032 | N |
| 3510294882898890880 | 8.23 | 0.75 | 343.2 | 3.891 | 2 | 0.049 | 0.033 | Y |
| 2075007556661946880 | 9.95 | 0.74 | 227.5 | 4.039 | 2 | 0.052 | 0.011 | N |
| 1342299192648782592 | 8.24 | 0.77 | 269.1 | 6.150 | 3 | 0.040 | 0.033 | N |
| 4761346872572913408 | 9.28 | 0.71 | 423.2 | 6.227 | 2 | 0.052 | 0.034 | N |
| 523313040665475968 | 11.23 | 1.13 | 375.8 | 7.573 | 2 | 0.015 | 0.048 | N |
| 4517777421819724416 | 9.91 | 0.91 | 201.0 | 7.840 | 2 | 0.053 | 0.021 | N |
| 1286024744429754752 | 11.22 | 1.54 | 218.4 | 8.600 | 2 | 0.009 | 0.047 | N |

relative to the primary is

$$\frac{F_2}{F_1} = 10^{-0.4\Delta G} = 0.0322. \tag{10}$$

GCNS identifies the pair as bound and gives a projected separation of 263.7 au. Both components fall within a single TESS pixel, so the 1.668-d signal is periodic photometric variability of the blended pair and cannot be attributed to either component with the present data. The system is therefore identified as the highest-priority follow-up target of the catalogue (Sect. 4).

### 3.3. Alias audit and association tests

Instrumental-period screening rejected numerous maxima that would otherwise appear significant. Of the 227 analysed sector light curves, 32 maxima occur near a low-order harmonic of the TESS orbital period, whereas 36 lie at a search boundary. Neither category contributes independently to a primary or secondary candidate. Their locations relative to accepted and other candidate peaks are shown in Fig. 6.

None of the tested period associations reaches statistical significance. Spearman coefficients for $v_{\rm LSR}$, Gaia colour, and absolute $G$ magnitude are $\rho = 0.142$, 0.092, and 0.070, respectively, with a common Benjamini–Hochberg-adjusted value of $p = 0.744$. Candidates of either tier occur in six of 15 targets carrying a multiplicity indicator (40.0 per cent) and in 18 of 83 without one (21.7 per cent). Although the corresponding odds ratio is 2.41, a two-sided Fisher exact test gives $p = 0.189$. The difference is therefore not statistically significant, and the comparison is reported as an exploratory result only (Table 3).

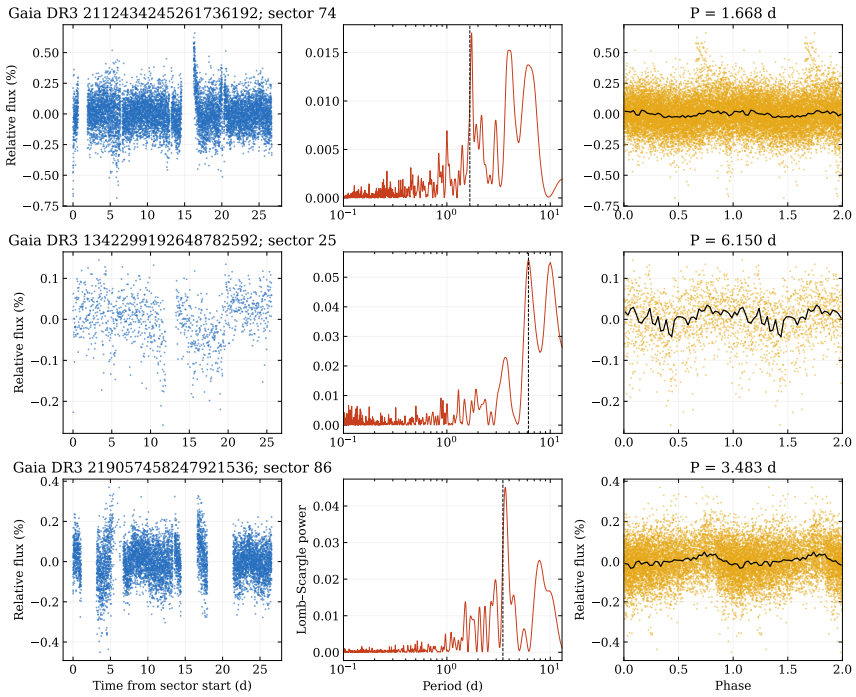



**Figure 5.** Sector light curves, periodograms, and phase-folded results for representative primary candidates, including the 1.668-d system. The panels support the periodic–variability classification but do not identify which component of an unresolved system is modulated.

### 3.4. Injection–recovery sensitivity

Recovery fractions from the indicative injection experiment on eight light curves are presented in Fig. 7. Throughout the 0.25–5 d test interval, amplitude is the dominant determinant of recovery: rates across the period grid remain between 0 and 30 per cent for fractional semi-amplitudes of 0.001–0.01 per cent, increase to 77.5–85 per cent at 0.03 per cent, and reach 100 per cent at 0.1 per cent. Consequently, the adopted pipeline has high sensitivity to the tested short-period sinusoids near and above a 0.03 per cent semi-amplitude in these light curves, while becoming markedly incomplete below 0.01 per cent.

## 4. Discussion

Among the 98 targets of the brightness-prioritised TESS subsample, 14 display period agreement across multiple sectors and constitute the primary candidates.

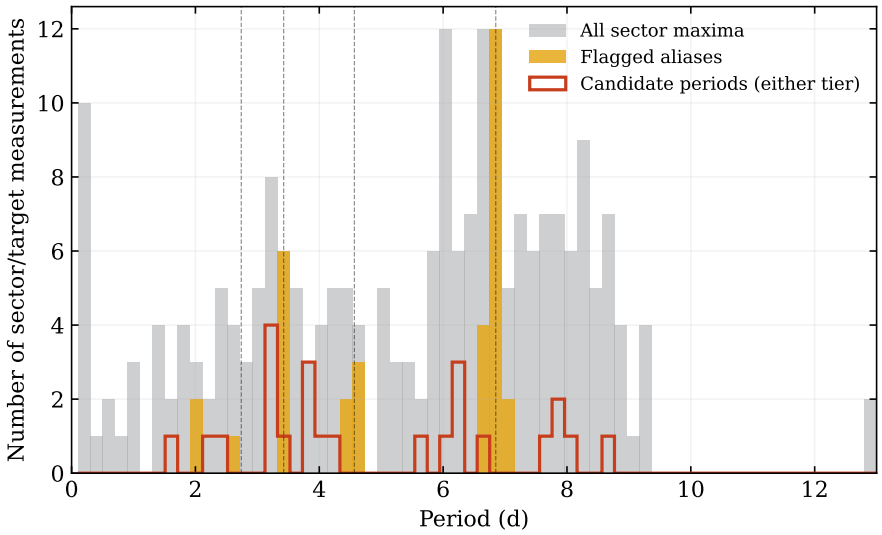



**Figure 6.** Sector-level period audit. Maxima near harmonics of the spacecraft orbital period or at the search boundaries are shown separately from the accepted candidate periods of either tier.

**Table 3.** Exploratory association tests. Period correlations use the 24 candidates of both tiers; the multiplicity comparison uses all 98 targets of the TESS subsample.

| Comparison | $N$ | Statistic | $p$ (BH) |
|---|---|---|---|
| period vs $v_{\mathrm{LSR}}$ speed | 24 | $\rho = 0.142$ | 0.744 |
| period vs $G_{\mathrm{BP}} - G_{\mathrm{RP}}$ | 24 | $\rho = 0.092$ | 0.744 |
| period vs absolute $G$ | 24 | $\rho = 0.070$ | 0.744 |
| Multiplicity vs candidate detection | 98 | OR = 2.41 | 0.189 |

Ten further objects show strong but single-sector signals and constitute the secondary candidates. Keeping those detections in a separate tier preserves potentially useful follow-up targets without assigning them the same empirical support as repeated signals. Because the subsample was drawn from the brightest 100 of the 182 parent-sample stars, the yields quoted in Sect. 3 characterise that magnitude-selected subsample only and should not be read as the periodic-variable fraction of the complete high-velocity population.

Candidate periods cover 1.668–8.600 d, yet only one of the 24 candidates of both tiers lies below 2 d. Such scarcity of very short periods resembles the behaviour reported for kinematically old nearby M dwarfs (Giacobbe et al., 2020). Each period is, however, a measurement of the combined light in a TESS aperture. A periodic photometric signal does not by itself establish a stellar

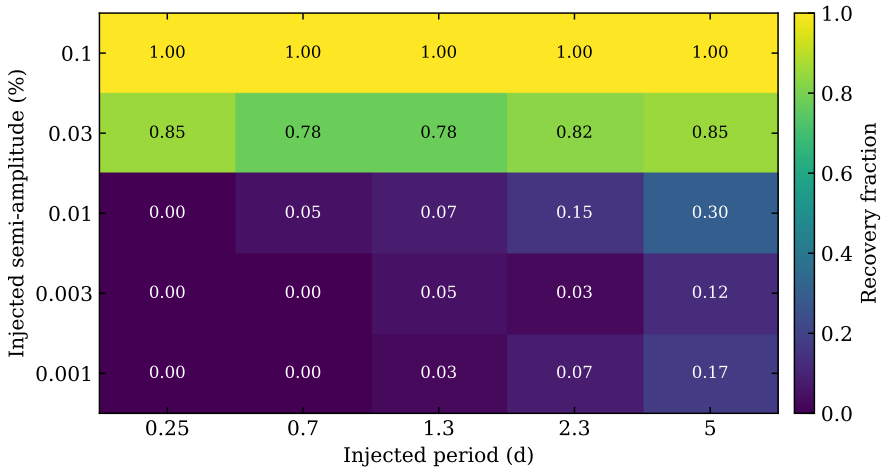



**Figure 7.** Recovery fraction for sinusoids injected into eight real TESS residual light curves. The experiment preserves the observed sampling and residual noise; each cell combines 40 trials. The result is an indicative sensitivity test of the pipeline rather than a population completeness model.

rotation period, particularly where binarity or unresolved contamination is possible, so the catalogue entries are rotation candidates rather than measured rotation periods. Within the present catalogue, the exceptional short-period system is the most direct target for resolving the origin of rapid modulation.

Its 1.668-d period recurs in two sectors, but a fainter Gaia companion shares the TESS aperture. On the basis of the $G$-band magnitude difference, that source contributes about 3.2 per cent of the target flux; the projected pair separation is approximately 264 au, and both sources fall within the same TESS pixel. The signal is therefore attributed to the unresolved pair, and the system is identified as the principal follow-up target of this study. Resolved time-series photometry, component-by-component spectroscopy, and pixel-level light-curve analysis could locate the variable member and clarify the modulation mechanism.

Multiplicity-flagged targets yield a higher nominal detection fraction than the remaining sample (40.0 versus 21.7 per cent), corresponding to an odds ratio of 2.41. With $p = 0.189$ in the Fisher exact test, however, the difference is not statistically significant, and the current counts do not establish an association between multiplicity and periodic variability. The comparison is exploratory. It provides an effect-size estimate that can inform a larger experiment using a uniform binary indicator, not evidence for a correlation.

Injection–recovery tests place the transition to high sensitivity near a semi-amplitude of 0.03 per cent for the trial short-period sinusoids, with a rapid decline

at lower amplitudes. This experiment rests on eight representative residual light curves and one signal shape, so it is an indicative sensitivity test of the adopted pipeline rather than a complete population-level completeness analysis; the limitation is discussed further below. Alias screening is comparably important: 32 sector maxima coincide with harmonics of the TESS orbital timescale, and 36 more occur at a search boundary. Cross-sector consistency, alias control, and empirical sensitivity therefore supply complementary evidence. By recording each element rather than only a preferred period, the catalogue supports transparent selection for resolved photometric and spectroscopic follow-up.

### 4.1. Relation to Gaia DR3–LAMOST high-velocity-star studies

Gaia DR3 kinematics have been combined with LAMOST spectroscopy to characterise high-velocity stars over a far larger volume than the one studied here. Elsanhoury (2025) analysed three high-velocity programmes containing 591, 87, and 519 stars at distances from about 0.1 to 109 kpc, deriving their $(U, V, W)$ velocities, velocity-ellipsoid dispersions, convergent points, solar motion, Oort constants, and mean Galactic rotation velocity. In our earlier work (Li et al., 2026), three published Gaia–LAMOST high-velocity-star catalogues were reassessed and the unbound classification of their candidates was shown to depend chiefly on the adopted distance estimator; the final strict sample of that study contains 356 stars. Both studies treat high-velocity stars as kinematic tracers and draw their membership from spectroscopic-survey catalogues.

The present work differs in sample, observable, and objective. The sample is volume-limited to the GCNS 100-pc sphere, is selected from GCNS and Gaia DR3 alone, and contains no LAMOST measurements; its Gaia DR3 source identifiers share no entry with the 356-star strict sample of Li et al. (2026). The observable is TESS time-series photometry of the individual stars rather than their space motions, and the endpoint is a validated periodic-variability catalogue rather than velocity-ellipsoid parameters or unbound probabilities. The two approaches are complementary. Population-level kinematic studies describe where high-velocity stars are and how they move, whereas the present catalogue asks what the nearest, brightest members of that population do photometrically on timescales of days. Extending the TESS analysis to spectroscopically characterised samples such as those of Elsanhoury (2025) would add the metallicity and abundance information that the present kinematic selection lacks.

### 4.2. Limitations

Because archive retrieval was prioritised by brightness, the TESS subsample contains 98 of the 182 kinematic candidates, and the reported yields describe that subsample only. They should not be interpreted as the periodic-variable fraction of the full 182-star high-velocity population, whose 84 fainter members remain unsearched. A low-velocity comparison sample matched in colour, absolute

and apparent magnitude, sky position, and TESS coverage would enable a direct population-level comparison. In this work, "high velocity" denotes the operational space-motion threshold $v_{\rm LSR} \geq 180\,{\rm km\,s^{-1}}$ applied with RUWE $<$ 2.0; spectroscopy can later add ages, metallicities, and chemical-population information.

At TESS resolution, close pairs contribute combined light to a common aperture. Product matching within 3 arcsec links a catalogue target to the intended data product, whereas source-level attribution requires finer spatial resolution. Both Gaia components of the 1.668-d system occupy one TESS pixel, making resolved photometry and spectroscopy especially valuable. Additional observing epochs would likewise determine whether the secondary-tier, single-sector signals recur.

Resolved companions, radial-velocity variability, and non-single-star solutions enter the multiplicity indicator through different selection channels, so its present role is exploratory. A consistently defined binary selection function and a larger sample would permit a more direct test of the multiplicity–variability relation. Similarly, the Lomb–Scargle search over 0.1–13 d is tuned to coherent, approximately sinusoidal short-period modulation; eclipses, flares, and longer rotation periods call for dedicated time-domain analyses. Eight representative light curves establish the amplitude scale of the present injection–recovery test, which is therefore an indicative sensitivity test of the adopted pipeline rather than a complete population-level completeness analysis. Extending the ensemble across the full range of target properties and spot morphologies would turn that diagnostic into a population completeness model.

## 5. Conclusions

Combining the GCNS parent catalogue with updated Gaia DR3 kinematics produced a parent sample of 182 nearby high-velocity dwarf candidates with $v_{\rm LSR} \geq 180\,{\rm km\,s^{-1}}$ and RUWE $< 2.0$. A brightness-prioritised archive search retrieved usable TESS light curves for a 98-target subsample. Within that subsample, period validation identified 14 primary candidates with multi-sector-consistent periods and ten secondary candidates with strong single-sector signals, over 1.668–8.600 d. The two tiers carry different levels of confirmation: repeated signals form the primary result, and strong signals lacking a second sector are reported separately for future observations. The corresponding yields describe the TESS-observed subsample and not the full parent sample.

All detected periods are reported as periodic photometric variability; they identify rotation candidates rather than measured rotation periods. One primary candidate lies below 2 d. Its 1.668-d signal appears in two sectors, but a Gaia companion at 2.76 arcsec shares the TESS aperture, so the system is flagged as the principal follow-up target. No significant association emerges between candidate period and LSR velocity, Gaia colour, or absolute $G$ magnitude, and

an exploratory multiplicity comparison (odds ratio 2.41, Fisher $p = 0.189$) is not statistically significant. For the injected short-period signals, the indicative sensitivity test shows high recovery near a 0.03 per cent semi-amplitude and substantial incompleteness below 0.01 per cent. The resulting catalogue combines period measurements with explicit evidence tiers and offers a practical target list for resolved photometry, pixel-level analysis, and spectroscopic follow-up.

**Acknowledgements.** We thank the anonymous referee, whose careful report improved the clarity and the scope statements of this paper.

This work has made use of data from the European Space Agency (ESA) mission *Gaia* (https://www.cosmos.esa.int/gaia), processed by the *Gaia* Data Processing and Analysis Consortium (DPAC, https://www.cosmos.esa.int/web/gaia/dpac/consortium). Funding for the DPAC has been provided by national institutions, in particular the institutions participating in the *Gaia* Multilateral Agreement.

This paper includes data collected by the TESS mission, which are publicly available from the Mikulski Archive for Space Telescopes (MAST) at the Space Telescope Science Institute. Funding for the TESS mission is provided by the NASA Explorer Program.

This research made use of Astropy, a community-developed core Python package for astronomy (Astropy Collaboration et al., 2022), and of Lightkurve, a Python package for Kepler and TESS data analysis (Lightkurve Collaboration et al., 2018).

## Data availability

The source catalogues are publicly available from the Gaia Archive, the GCNS data release, and the Mikulski Archive for Space Telescopes. The core analysis code and the machine-readable counterpart of Table A1 are openly available at https://github.com/Harry33t/gcns-tess-periodic-variability, the candidate catalogue as the file `data/tableA1_periodic_candidates.csv`. Remaining derived tables and cached query products can be provided by the corresponding author.

## References

Aigrain, S., Llama, J., Ceillier, T., et al., Testing the Recovery of Stellar Rotation Signals from Kepler Light Curves Using a Blind Hare-and-Hounds Exercise. 2015, *Monthly Notices of the Royal Astronomical Society*, **450**, 3211, DOI:10.1093/mnras/stv853

Angus, R., Aigrain, S., Foreman-Mackey, D., & McQuillan, A., Calibrating Gyrochronology Using Kepler Asteroseismic Targets. 2015, *Monthly Notices of the Royal Astronomical Society*, **450**, 1787, DOI:10.1093/mnras/stv423

Astropy Collaboration, Price-Whelan, A. M., Lim, P. L., et al., The Astropy Project: Sustaining and Growing a Community-oriented Open-source Project and the Latest Major Release (v5.0) of the Core Package. 2022, *The Astrophysical Journal*, **935**, 167, DOI:10.3847/1538-4357/ac7c74

Baluev, R. V., Assessing the Statistical Significance of Periodogram Peaks. 2008, *Monthly Notices of the Royal Astronomical Society*, **385**, 1279, DOI:10.1111/j.1365-2966.2008.12689.x

Barnes, S. A., Ages for Illustrative Field Stars Using Gyrochronology: Viability, Limitations, and Errors. 2007, *The Astrophysical Journal*, **669**, 1167, DOI:10.1086/519295

Binks, A. S. & Günther, H. M., tessilator: a one-stop shop for measuring TESS rotation periods. 2024, *Monthly Notices of the Royal Astronomical Society*, **533**, 2162, DOI:10.1093/mnras/stae1850

Binks, A. S., Jeffries, R. D., Sacco, G. G., et al., The Gaia-ESO survey: constraining evolutionary models and ages for young low-mass stars with measurements of lithium depletion and rotation. 2022, *Monthly Notices of the Royal Astronomical Society*, **513**, 5727, DOI:10.1093/mnras/stac1245

Elsanhoury, W. H., Kinematics of high-velocity stars utilizing LAMOST and Gaia DR3 archives within 100 kpc. 2025, *Contributions of the Astronomical Observatory Skalnaté Pleso*, **55**, 38, DOI:10.31577/caosp.2025.55.1.38

Gaia Collaboration, Smart, R. L., Sarro, L. M., et al., Gaia Early Data Release 3: The Gaia Catalogue of Nearby Stars. 2021, *Astronomy & Astrophysics*, **649**, A6, DOI:10.1051/0004-6361/202039498

Gaia Collaboration, Vallenari, A., Brown, A. G. A., et al., Gaia Data Release 3: Summary of the content and survey properties. 2023, *Astronomy & Astrophysics*, **674**, A1, DOI:10.1051/0004-6361/202243940

Giacobbe, P., Benedetto, M., Damasso, M., et al., Photometric rotation periods for 107 M dwarfs from the APACHE survey. 2020, *Monthly Notices of the Royal Astronomical Society*, **491**, 5216, DOI:10.1093/mnras/stz3364

Handberg, R., Lund, M. N., White, T. R., et al., TESS Data for Asteroseismology: Photometry. 2021, *The Astronomical Journal*, **162**, 170, DOI:10.3847/1538-3881/ac09f1

Huang, C. X., Vanderburg, A., Pál, A., et al., Photometry of 10 Million Stars from the First Two Years of TESS Full Frame Images: Part II. 2020, *Research Notes of the American Astronomical Society*, **4**, 206, DOI:10.3847/2515-5172/abca2d

Jenkins, J. M., Twicken, J. D., McCauliff, S., et al., The TESS Science Processing Operations Center. 2016, *Proceedings of SPIE*, **9913**, 99133E, DOI:10.1117/12.2233418

Katz, D., Sartoretti, P., Guerrier, A., et al., Gaia Data Release 3: Properties and validation of the radial velocities. 2023, *Astronomy & Astrophysics*, **674**, A5, DOI:10.1051/0004-6361/202244220

Li, F., Huang, G., & Yang, L., A Gaia DR3–LAMOST reassessment of high-velocity star candidates with geometric-distance-aware kinematics. 2026, *Contributions of the Astronomical Observatory Skalnaté Pleso*, **56**, 35, DOI:10.31577/caosp.2026.56.3.35

Lightkurve Collaboration, Cardoso, J. V. d. M., Hedges, C., et al. 2018, Lightkurve: Kepler and TESS time series analysis in Python, Astrophysics Source Code Library, ascl:1812.013

Lomb, N. R., Least-Squares Frequency Analysis of Unequally Spaced Data. 1976, *Astrophysics and Space Science*, **39**, 447, DOI:10.1007/BF00648343

Mamajek, E. E. & Hillenbrand, L. A., Improved Age Estimation for Solar-Type Dwarfs Using Activity–Rotation Diagnostics. 2008, *The Astrophysical Journal*, **687**, 1264, DOI:10.1086/591785

McQuillan, A., Mazeh, T., & Aigrain, S., Rotation Periods of 34,030 Kepler Main-Sequence Stars: The Full Autocorrelation Sample. 2014, *The Astrophysical Journal Supplement Series*, **211**, 24, DOI:10.1088/0067-0049/211/2/24

Newton, E. R., Irwin, J., Charbonneau, D., et al., The Rotation and Galactic Kinematics of Mid M Dwarfs in the Solar Neighborhood. 2016, *The Astrophysical Journal*, **821**, 93, DOI:10.3847/0004-637X/821/2/93

Ramsay, G., Doyle, J. G., & Doyle, L., TESS observations of southern ultrafast rotating low-mass stars. 2020, *Monthly Notices of the Royal Astronomical Society*, **497**, 2320, DOI:10.1093/mnras/staa2021

Ricker, G. R., Winn, J. N., Vanderspek, R., et al., Transiting Exoplanet Survey Satellite. 2015, *Journal of Astronomical Telescopes, Instruments, and Systems*, **1**, 014003, DOI:10.1117/1.JATIS.1.1.014003

Scargle, J. D., Studies in Astronomical Time Series Analysis. II. Statistical Aspects of Spectral Analysis of Unevenly Spaced Data. 1982, *The Astrophysical Journal*, **263**, 835, DOI:10.1086/160554

Schönrich, R., Binney, J., & Dehnen, W., Local kinematics and the local standard of rest. 2010, *Monthly Notices of the Royal Astronomical Society*, **403**, 1829, DOI:10.1111/j.1365-2966.2010.16253.x

Skumanich, A., Time Scales for CA II Emission Decay, Rotational Braking, and Lithium Depletion. 1972, *The Astrophysical Journal*, **171**, 565, DOI:10.1086/151310

Smith, J. C., Stumpe, M. C., Van Cleve, J. E., et al., Kepler Presearch Data Conditioning II—A Bayesian Approach to Systematic Error Correction. 2012, *Publications of the Astronomical Society of the Pacific*, **124**, 1000, DOI:10.1086/667697

Stassun, K. G., Oelkers, R. J., Paegert, M., et al., The Revised TESS Input Catalog and Candidate Target List. 2019, *The Astronomical Journal*, **158**, 138, DOI:10.3847/1538-3881/ab3467

Stumpe, M. C., Smith, J. C., Van Cleve, J. E., et al., Kepler Presearch Data Conditioning I—Architecture and Algorithms for Error Correction in Kepler Light Curves. 2012, *Publications of the Astronomical Society of the Pacific*, **124**, 985, DOI:10.1086/667698

van Saders, J. L., Ceillier, T., Metcalfe, T. S., et al., Weakened Magnetic Braking as the Origin of Anomalously Rapid Rotation in Old Field Stars. 2016, *Nature*, **529**, 181, DOI:10.1038/nature16168

VanderPlas, J. T., Understanding the Lomb–Scargle Periodogram. 2018, *The Astrophysical Journal Supplement Series*, **236**, 16, DOI:10.3847/1538-4365/aab766

**Table A1.** Catalogue of all 24 periodic-variability candidates. Class 'multi' denotes primary (multi-sector) candidates; class 'single' denotes secondary (strong-single-sector) candidates, which carry a lower level of confirmation.

| Gaia DR3 source ID | RA | Dec. | $G$ | $v_{\rm LSR}$ | $P$ | Semi-amp. | Class | RUWE | Mult. |
|---|---|---|---|---|---|---|---|---|---|
| 2112434245261736192 | 273.149 | 40.555 | 10.66 | 183.2 | 1.668 | 0.025 | multi | 0.89 | Y |
| 1080623048803799040 | 173.099 | 76.652 | 11.32 | 308.5 | 2.265 | 0.028 | multi | 1.01 | N |
| 6480032187014809600 | 316.911 | -47.322 | 10.06 | 272.8 | 2.344 | 0.019 | multi | 1.30 | N |
| 5380306876026603648 | 179.612 | -41.923 | 8.67 | 190.3 | 3.169 | 0.023 | multi | 1.02 | Y |
| 5817597047142573952 | 252.922 | -64.441 | 10.70 | 369.7 | 3.182 | 0.019 | multi | 1.14 | N |
| 219057458247921536 | 60.822 | 35.267 | 8.23 | 182.0 | 3.483 | 0.024 | multi | 1.01 | N |
| 1752459532807704704 | 306.550 | 9.448 | 8.21 | 270.5 | 3.753 | 0.032 | multi | 0.92 | N |
| 3510294882898890880 | 193.314 | -18.526 | 8.23 | 343.2 | 3.891 | 0.033 | multi | 1.03 | Y |
| 2075007556661946880 | 302.257 | 42.867 | 9.95 | 227.5 | 4.039 | 0.011 | multi | 0.88 | N |
| 1342299192648782592 | 264.901 | 37.180 | 8.24 | 269.1 | 6.150 | 0.033 | multi | 0.83 | N |
| 4761346872572913408 | 78.280 | -59.643 | 9.28 | 423.2 | 6.227 | 0.034 | multi | 0.84 | N |
| 523313040665475968 | 17.124 | 63.515 | 11.23 | 375.8 | 7.573 | 0.048 | multi | 0.91 | N |
| 4517777421819724416 | 285.179 | 19.072 | 9.91 | 201.0 | 7.840 | 0.021 | multi | 0.92 | N |
| 1286024744429754752 | 220.141 | 31.476 | 11.22 | 218.4 | 8.600 | 0.047 | multi | 1.20 | N |
| 222749343414443648 | 52.228 | 37.378 | 10.50 | 256.6 | 3.209 | 0.074 | single | 1.23 | N |
| 1159108770069883136 | 220.821 | 5.828 | 10.29 | 358.0 | 3.284 | 2.730 | single | 1.18 | Y |
| 6859076107589173120 | 305.902 | -21.375 | 8.50 | 302.0 | 3.851 | 0.015 | single | 1.01 | N |
| 235423517026072960 | 49.116 | 38.094 | 10.17 | 246.4 | 4.221 | 0.066 | single | 1.25 | N |
| 3284151179589287680 | 66.446 | 5.266 | 11.45 | 210.7 | 5.568 | 0.050 | single | 0.78 | N |
| 112440873718983680 | 47.106 | 26.327 | 7.90 | 209.9 | 5.966 | 0.007 | single | 1.01 | N |
| 6307365499463905536 | 227.549 | -16.479 | 9.16 | 594.1 | 6.218 | 0.026 | single | 1.21 | Y |
| 615943806835727872 | 147.235 | 13.741 | 8.21 | 301.6 | 6.614 | 0.029 | single | 1.10 | N |
| 170216567626711296 | 61.553 | 32.947 | 9.65 | 197.0 | 7.889 | 4.626 | single | 0.97 | N |
| 6307374845312759552 | 227.550 | -16.395 | 8.83 | 594.0 | 8.038 | 0.014 | single | 0.93 | Y |

**Table A2.** Injection–recovery fractions for representative TESS light curves. Amplitudes are injected sinusoidal semi-amplitudes.

| Semi-amp. (%) | 0.25 d | 0.7 d | 1.3 d | 2.3 d | 5.0 d |
|---|---|---|---|---|---|
| 0.001 | 0.0 | 0.0 | 2.5 | 7.5 | 17.5 |
| 0.003 | 0.0 | 0.0 | 5.0 | 2.5 | 12.5 |
| 0.010 | 0.0 | 5.0 | 7.5 | 15.0 | 30.0 |
| 0.030 | 85.0 | 77.5 | 77.5 | 82.5 | 85.0 |
| 0.100 | 100.0 | 100.0 | 100.0 | 100.0 | 100.0 |